

## INFLUENCE OF PRINCIPAL STRESS DIRECTION ON THE STRESS-STRAIN BEHAVIOUR OF COMPLETELY DECOMPOSED GRANITE

Md. Kumruzzaman<sup>1\*</sup>, Jian-Hua Yin<sup>2</sup>

<sup>1</sup>Department of Civil Engineering

Rajshahi University of Engineering & Technology, Bangladesh

<sup>2</sup>Department of Civil and Structural Engineering

The Hong Kong Polytechnic University, Hung Hom, Kowloon, Hong Kong, China

\*Corresponding author: kzzaman2001@hotmail.com

---

**Abstract :** The measurement and study of the stress-strain-strength behavior of soils in general stress states involving principal stress rotation are necessary and valuable. To investigate the strength behavior under principal stress rotation, a series of undrained tests on compacted hollow cylinder specimens of completely decomposed granite (CDG) was carried in hollow cylinder apparatus. Tests were conducted at constant inside and outside pressures and maintained a fixed angle of rotation of principal stress with the vertical ( $\alpha$ ). Seven different angles of major principal stress orientations were used to cover the entire range of major principal stress directions from vertical to the horizontal. Two different confining stresses were also used. It is observed that the deviator stresses as well as excess pore pressures decrease with the angle  $\alpha$ . It is also observed that specimens were getting softer with the increase of  $\alpha$ . The results also show a significant influence of principal stress direction angle on the strength parameters. It is found that the angle  $\alpha$  is related to the occurrence of cross-anisotropy and the localization which resulted in a pronounced influence on the strength parameters of the CDG specimens.

**Keywords :** *Hollow cylinder; principal stress rotation; friction angle; failure surface; cross anisotropy*

### 1.0 Introduction

Rotation of principal stress directions are common features in many geotechnical engineering problems and may have significant influences on the behavior of soils. Axial-torsional loading on hollow cylinder specimens can better simulate this condition in the laboratory. Broms and Casbarian (1965) first investigated the effects of the rotation of principal stress axes on the shear strength and pore pressure in kaolin clay. Experimental findings revealed that the rotation of principal stress causes the increase of pore pressure coefficient as

well as the decrease of deviator stresses. Similar to Broms and Casbarian (1965), Saada and Zamini (1973) found that the effective stress paths, pore pressure coefficients and the effective friction angles are functions of the inclination of the principal stresses for kaolin clay. In addition to the experimental results, Saada and Townsend (1980) explained the state of stresses in hollow cylinder specimens under axial-torsional loading and described the stress non-uniformities in the hollow cylinder specimens. It was recommended to use the appropriate dimensions of the specimen to avoid the nonuniform stresses. Saada (1988) further described the advantages and limitations of testing a hollow cylinder specimen under axial-torsional loading. The effect of principal stress rotation on kaolin clay was also investigated by Hong and Lade (1989). The experimental results concluded that the isotropic elasto-plastic theory may be suitable to model  $K_0$  consolidated clay during principal stress rotation. Lin and Penumadu (2005) presented the effective friction angles, undrained shear strengths, stress-strain relationships, pore water pressures and stress-paths as a function of the angle of principal stress rotation. Strong anisotropy for kaolin specimens under principal stress rotation was also concluded using the experimental results.

Albert et al. (2003) conducted rotation of principal stresses on Bothkennar clay and found that the effective stress paths are not very brittle as those observed in triaxial compression tests. It was also pointed out that the shearing resistance from torsional shear tests is similar to the values that obtained in triaxial compression and extension tests. Lade et al. (2008) performed stress rotation tests on Santa Monica beach sand. It is concluded that the strength parameters are influenced by the cross-anisotropic behavior of sand as well as shear banding. Most of the previous test studies were carried out on sedimentary soils like sand and clay. Less previous study has been done to investigate the influence of the principal stress rotation on the stress-strain behavior of residual soils which are abundant in many countries and regions, for example; Malaysia, Japan, Korea, Hong Kong, Taiwan, USA.

In Hong Kong, approximately 90% of the rock is granite. The weathering of the granite in situ produced a lot of Completely Decomposed Granite (CDG) soils, for examples, in most soil slopes in Hong Kong. The CDG soils may be cut and used as fill materials (compacted) for land formation works, marine reclamations, as back fills of retaining walls, *etc.* Therefore, re-compacted CDG soils are often encountered in most of infrastructural projects, building projects, and slope stabilization project. As pointed out before, normally these CDG soils are subjected to a rotation of principal stress. Therefore, the measurement and study of the stress-strain-strength behavior of CDG soils in 3-D stress states are necessary and of academic interests and importance.

This paper presents an experimental study to investigate the influence of principal stress directions on the stress–strain and strength behavior of completely decomposed granite (CDG) of Hong Kong. Distribution of stresses and the rotation of principal stress on hollow cylinder specimen are shown in Figure 1. Tests have been performed using a hollow cylinder testing system that has been developed by Geotechnical Consulting and Testing System (GCTS, 2007). The results of consolidated undrained tests with various principal stress directions on completely decomposed granite (CDG) are presented and discussed.

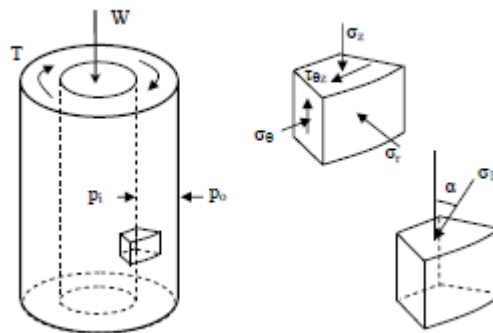


Figure 1: Elements in a hollow cylinder specimen with forces, pressures and stresses

## 2.0 Testing Apparatus and Specimen

The hollow cylinder apparatus that has been employed in this testing program are developed by **GCTS**. The apparatus comprises of axial-torsional loading system, pressure controllers, triaxial cell, and the electronic system. The axial torsional loading system and pressure system are briefly described below.

### 2.1 Axial-Torsional Loading

The axial-torsional loading system is shown in Fig.2. The loading frame is relatively light weight but highly stable and has a small tabletop footprint. The cross head beam supports the double acting load cylinders used to apply the axial load and torque. These two GCTS loaders offer low start up pressure, extreme sensitive response, very low friction and low breakaway force for smooth action.

These loaders are servo electro-actuated with hydraulic pressure. The loading system is capable of applying axial load or torque separately or both of them simultaneously. The maximum load of 22.25 kN and the maximum torque of 225 N-m can be applied by using this loading system. The loading platens (Figure 2) are the interface between the pressure /volume control unit and the testing specimen. The loading platens can accommodate a specimen having the dimensions: 200 mm in height, 100 mm in outer diameter and 50 mm in inner diameter. Each of the loading platens (cap and base) has eight porous disks (14mm in diameter) and eight lips (1.7mm in width and 3 mm in height), those can make the specimens saturated and can produce the smooth torque without any slippage.



Figure : Loading frame and triaxial cell for HCA

## 2.2 Pressurization System

The pressurization system (Figure 3) consists of five electro-hydraulically actuated computer servo controlled pressure/volume controllers, transducers for the direct measurements of volumes and pressures. The five controllers are responsible for the outer cell pressure, inner cell pressure, top back pressure, bottom back pressure and base pore water pressure. The system utilizes the hydraulic digital servo control for maintaining necessary test conditions. Each pressure/volume controller has a capacity of 280 cc and is capable of providing controls and measurements of volume changes as small as 0.01cc. The maximum pressure of 1000kPa can be applied through these pressure controllers that are accurate to pressure of 0.1 kPa. The pressure transducer and an external **LVDT** supply a direct feedback response used in the control process. System operation is integrated with the easy to use *CATS* (GCTS 2007) software which has the flexibility to follow simple or complex test conditions.

All the parameters that need to control for maintaining the fixed principal stress orientations are worked with **PID** control system. So the control achievement is good enough and PID control makes almost accurate adjustments of the stresses. The advantages of PID controls have been discussed briefly by Mandeville and Penumadu (2004).



Figure 3: Pressure system for hollow cylinder apparatus

### 2.3 Basic Properties of Completely Decomposed Granite

The Completely Decomposed Granite (CDG) soil used in this study was taken from a slope site in Hong Kong. Specific gravity tests, particle size distribution tests, Atterberg limit tests, and standard compaction tests were done on the disturbed CDG soil. The percentage of soils finer than the No.200 sieve is about 52%. According to the Unified Soil Classification System (USCS), the CDG soil is classified as CL. A summary of basic properties from these tests is presented in Table 1. The grain size distribution curve is shown in Figure 4. It is noted that the maximum dry density of  $1.80 \text{ Mg/m}^3$  was obtained by the standard compaction tests (using Proctor compaction tests). The dry density in the most compacted fill slopes is 95% of the maximum dry density, that is,  $1.71 \text{ Mg/m}^3$ . The dry density of  $1.71 \text{ Mg/m}^3$  (void ratio= 0.55) was used to prepare all specimens.

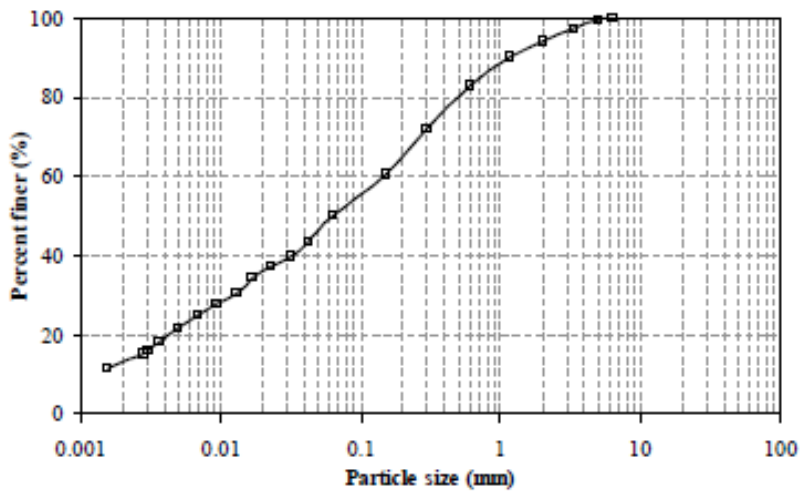


Figure 4. Particle size distribution curve for Completely Decomposed Granite (CDG)

Table 1: Properties of the completely decomposed granite fill

Parameters	Unit	Value
Specific gravity		2.65
The maximum dry density	Mg/m <sup>3</sup>	1.80
The optimum moisture content	%	15.5
Plastic limit	%	22.7
Liquid limit	%	32.8
Gravel content	%	1.0
Sand content	%	47.0
Fibe content	%	52.0

#### 2.4 Preparation of Specimens and Testing Procedures

Recompacted CDG soil specimens were used in this testing study. A split mould of inner diameter 100mm was used for the preparation of specimens. A rigid plastic bar of diameter 50mm was fixed with a gridded base plate. Wax was used to the inner surface of mold, outer surface of the plastic rod and the base plate before placing the split mould on the base plate. The CDG soil was compacted to 95% of the maximum dry density, that is, 1.71 Mg/m<sup>3</sup> with initial water content of 13% to 14%. The soil was compacted in seven layers in the mould following the procedure described in ASTM standard D4767-95. At first, the oven dried soil mass was mixed thoroughly with water and then divided into seven portions. Each portion of soil was then poured into the mould and was tamped gently to fill up the required volume. The top of each layer was scarified prior to the addition of material for the next layer. The tamper was used to compact the soil in layers inside the mould. After a specimen was formed, the inside plastic rod was pushed and taken it out. The specimen was placed on the base platen of the triaxial cell and the outer mould assemble was carefully removed from the specimen so that there is no disturbance of the specimens. The inner membrane was fixed to the base of the triaxial cell before placing the specimen. Placing of the top cap and filter strips, outer membrane was then fixed. The thickness of the rubber membrane was 0.35mm. Triaxial cell was then set by placing the top cover plate. It is noted that there were two drainage lines (opposite to each other) on the top cap which were connected to single drainage line for drainage of water to or from the top of the specimens. Figure 5 shows (a) split mould, solid plastic rod, the top and base of the mould (left side), (b) a specimen fully enclosed by rubber membrane with water tube connector (right side) for water drainage or water pressure measurement.



Figure 5: (a) Mold assembly for sample preparation (b) specimen placed in hollow cylinder triaxial cell

Setting the whole assemble of the triaxial cell, de-aired water was then used to flush from the bottom outlet and out of the upper outlet tube to remove entrapped air in the specimen while maintaining an effective confining cell pressure of 8 kPa (inner and outer cell pressure 15kPa and back pressure from the bottom of the specimen is 7kPa). The top drainage valve was open to remove the trapped air. After 3hrs flushing and passing water through the upper drainage, a back pressure of 200 kPa was applied in all the tests. Skempton's B-value of 0.96-0.98 was obtained for all specimens.

After saturation, specimens were then consolidated isotropically by applying the same inner and outer pressures. Two different consolidation pressures of 400 kPa and 200 kPa were used to consolidate the specimens in this experimental program. The step was followed up by a controlled stress path. Seven different stress paths with constant angles of principal stress rotation ( $\alpha$ ) of  $0^\circ$ ,  $23^\circ$ ,  $30^\circ$ ,  $45^\circ$ ,  $60^\circ$ ,  $67^\circ$  and  $90^\circ$  were carried out to observe the effect of principal stress rotation, by means of adjusting the vertical stress,  $\Delta\sigma_v$  and the shear stress,  $\Delta\tau$  so that  $2\alpha = \tan^{-1}(2\Delta\tau / \Delta\sigma_v)$  is kept a constant. With a same inner and outer pressure in a hollow specimen, combination of axial and torsional load can rotate the principal stress and introduce the coefficient of intermediate principal stress simultaneously. The relationship between principal stress direction with the vertical ( $\alpha$ ) and the coefficient of intermediate principal stress ( $b$ ) is expressed as;  $b = \sin^2 \alpha$ .

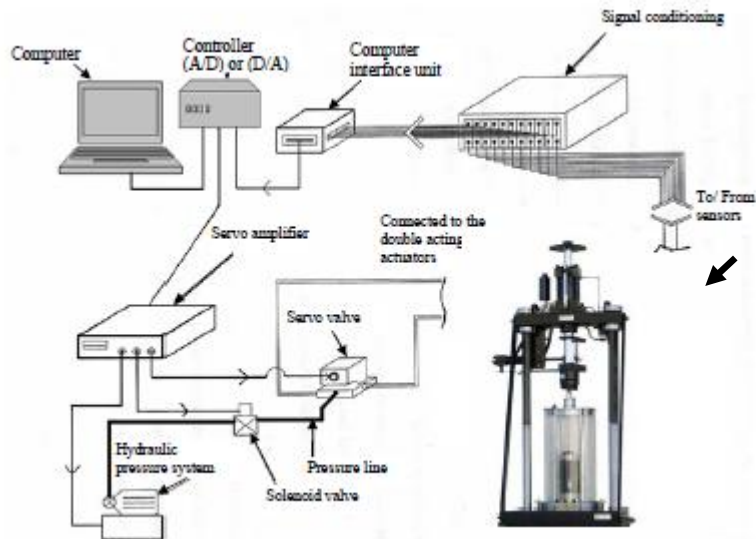


Figure 6: Setup of hollow cylinder system

Data acquisition and control loops were performed with updating intervals of 60 secs. Data from the experiments are logged electronically by a computer. All the transducers in the setup are connected to a controller through the computer interface unit for data acquisition and control. The controller itself is also connected to the computer. CATS software (GCTS, 2007) is used to automate various phases of testing such as saturation, consolidation, and application of stresses for applying a predetermined stress path or strain path. The setup of hollow cylinder system is shown schematically in Figure 6.

### 3.0 Stress and Strain Parameters

The specimens were isotropically consolidated by applying the same inner and outer pressures. The vertical load and torque were then applied on the specimens to rotate the major and minor principal stresses. The intermediate principal stress is always fixed to the horizontal direction and equal to the radial stress. The angle of major principal stress with the vertical,  $\alpha$  can be obtained by the equation:  $2\alpha = \tan^{-1}(2\Delta\tau / \Delta\sigma_v)$ .

Neglecting the membrane effects and considering the uniform distribution of stresses across the cross sectional area (Lin and Penumadu, 2002), the change of vertical stress and horizontal stresses were calculated as  $\Delta\sigma_v = W/A$  and  $\Delta\tau_{\theta z} =$

$3T/2\pi(r_o^3-r_i^3)$ , where  $W$  is the axial load,  $A$  the cross-sectional area of the specimen,  $T$  the torque applied on the specimen,  $r_o$  and  $r_i$  are the outer and inner radius respectively.

The principal stresses and the principal strains were calculated using the following equations presented in Saada and Townsend (1980) and further extended in Lin and Penumadu (2002):

$$[1] \left\{ \begin{array}{l} \Delta\sigma_1 = \Delta\sigma_v [1 + \sqrt{1 + 4k^2}] / 2 \\ \Delta\sigma_2 = 0 \\ \Delta\sigma_3 = \Delta\sigma_v [1 - \sqrt{1 + 4k^2}] / 2 \\ k = \Delta\tau / \Delta\sigma_v \\ \varepsilon_z = \Delta u_v / H_o \\ \varepsilon_r = 1 - \sqrt{[1/(1 - \varepsilon_z)]} \\ \varepsilon_\theta = \sqrt{[1/(1 - \varepsilon_z)]} - \varepsilon_z - 1 \\ \gamma_{\theta z} = \Delta\theta \cdot r_i / H_o (1 + \varepsilon_z) \\ \varepsilon_1 = \frac{\varepsilon_z + \varepsilon_\theta}{2} + \frac{1}{2} \sqrt{(\varepsilon_z - \varepsilon_\theta)^2 + (\gamma_{\theta z})^2} \\ \varepsilon_3 = \frac{\varepsilon_z + \varepsilon_\theta}{2} - \frac{1}{2} \sqrt{(\varepsilon_z - \varepsilon_\theta)^2 + (\gamma_{\theta z})^2} \end{array} \right.$$

Where,  $H_o$  is the initial height of the specimen.  $\Delta u_v$  and  $\Delta\theta$  are the change of vertical and angular displacements, respectively.

Experimental results for axial and torsional stresses were corrected with the real values of inner and outer radius. The realtime updated values of inner and outer radius ( $R_i$  and  $R_o$ ) during shearing were calculated using the equations used by Tatsuoka et al. (1986)

$$[2] \left\{ \begin{array}{l} R_o = \sqrt{\frac{1}{1 - \varepsilon_z}} r_o \\ R_i = \sqrt{\frac{1}{1 - \varepsilon_z}} r_i \end{array} \right.$$

where  $\varepsilon_z$  is the axial strain. The deviator stress and the mean stresses are calculated as the followings;

$$[3] \quad \begin{cases} q = \sqrt{\frac{(\sigma_1 - \sigma_2)^2 + (\sigma_2 - \sigma_3)^2 + (\sigma_3 - \sigma_1)^2}{2}} \\ p' = \frac{\sigma_1' + \sigma_2' + \sigma_3'}{3} \end{cases}$$

### 3.1 Loading paths

For  $\alpha=0^\circ$  and  $\alpha=90^\circ$ , a test was carried out in stress control mode with compression or extension at the same speed of 0.1 kN/hr while angular deformation was restrained. Restraining of angular deformation generated some torsional stresses and the values were about  $\pm 3.0$ kPa, which might be neglected in respect to larger compression (or extension) stresses (Lin and Penumadu 2005). For  $\alpha=45^\circ$ , vertical piston load was controlled to be zero value, while the torsional stress was applied at the rate of 4.7kPa/hour. Due to the zero piston loading control in a vertical direction, the loading ram moved and developed some axial strain after a little shear strain. Therefore, the stress and strain were not coaxial. For  $\alpha =23^\circ, 30^\circ, 60^\circ$  and  $67^\circ$ , vertical and shear stresses were applied as a proportion of  $k =\Delta\tau /\Delta\sigma_z$ . The controller of the hollow cylinder system precisely applied the predefined ratio of vertical and shear stresses. However, the strain paths for  $\alpha =23^\circ$  and  $30^\circ$  were not coincided with the stress paths. Therefore, non-coaxiality has also been observed for these two stress paths. As the compacted CDG is cross-anisotropic, the cross-anisotropic nature of compacted CDG probably affected the strain paths. In the case of  $\alpha = 60^\circ$  and  $67^\circ$ , such a deviation of strain paths was not found for the CDG. The control of the loading for  $\alpha=30^\circ$  and  $60^\circ$  are shown in Figure 7.

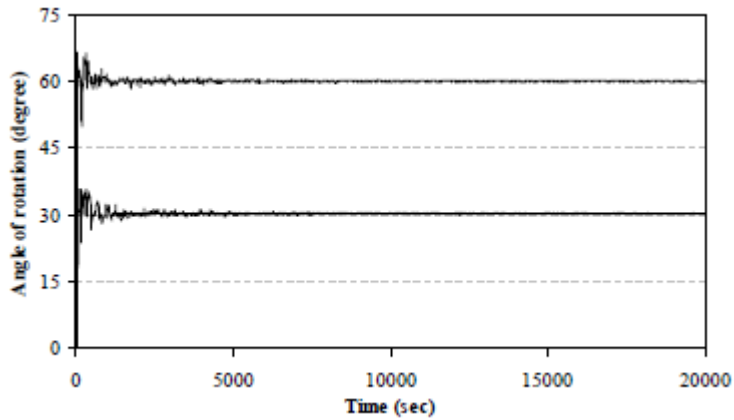


Figure 7: Directions of principal stresses for  $\alpha=30^\circ$  and  $60^\circ$  ( $p_c=400$  kPa)

#### 4.0 Test Results and Discussion

##### 4.1 Stress-Strain Behaviour

The main test results from a series of tests with different inclinations of major principal stress for two different consolidation stresses are presented and discussed in this section. Figure 8 shows measured curves of (a) normalized deviator stress ( $q/p_c$ ) versus shear strain ( $\epsilon_1 - \epsilon_3$ ), (b) normalized excess pore water pressure ( $\epsilon_v$ ) versus shear strain ( $\epsilon_1 - \epsilon_3$ ) and (c) effective stress paths ( $q-p'$  space) for  $\alpha$ -values of  $0^\circ$ ,  $23^\circ$ ,  $30^\circ$ ,  $45^\circ$ ,  $60^\circ$ ,  $67^\circ$ , and  $90^\circ$  respectively from consolidated undrained tests on the CDG soil specimen for the consolidation stress of 400 kPa. Fig.9 also shows the same types of curves from undrained hollow cylinder tests on the CDG soil specimen for  $p_c$  of 200 kPa. It shall be explained that curves in Figures 8 and 9 do not have data points since these curves are too close to each other in most regions. If data points were shown, any small difference of the curves could not be seen clearly.

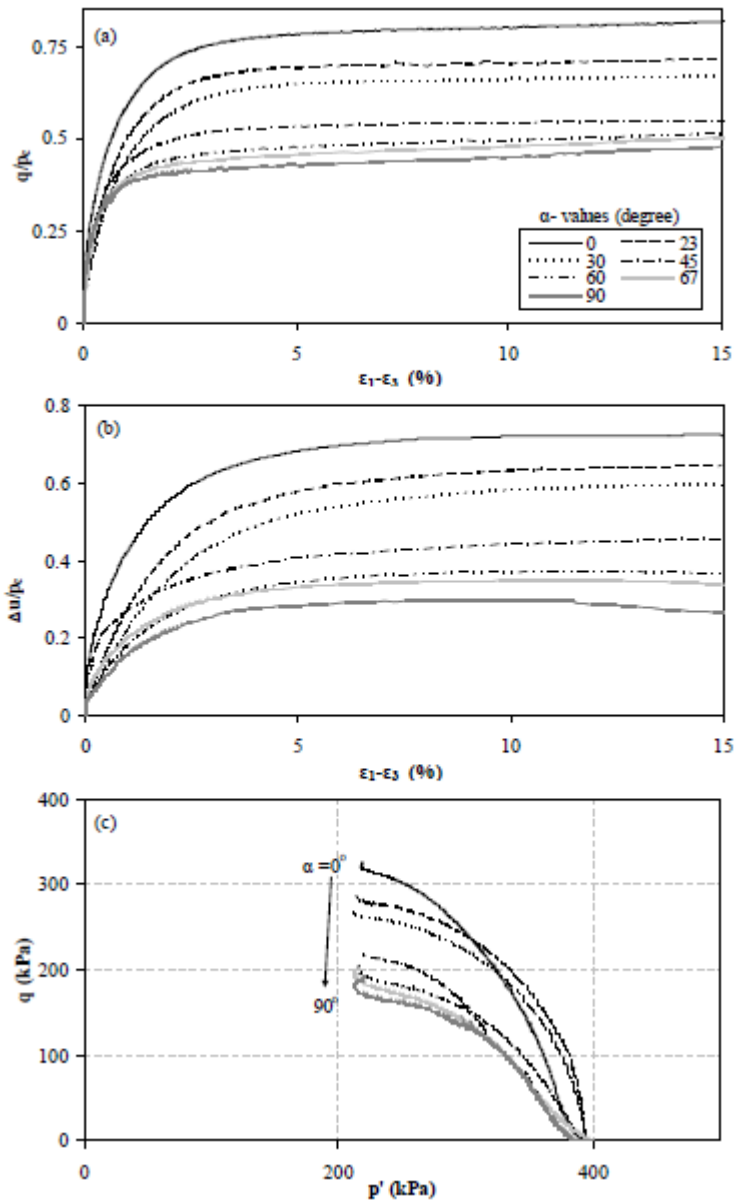


Figure 8: (a) normalized shear stress ( $q/k$ ) versus shear strain ( $\epsilon_1 - \epsilon_3$ ), (b) normalized excess pore water pressure ( $\Delta u/k$ ) versus shear strain ( $\epsilon_1 - \epsilon_3$ ), and (c) effective stress path ( $q$  vs.  $p'$ ) for consolidation pressure of 400 kPa

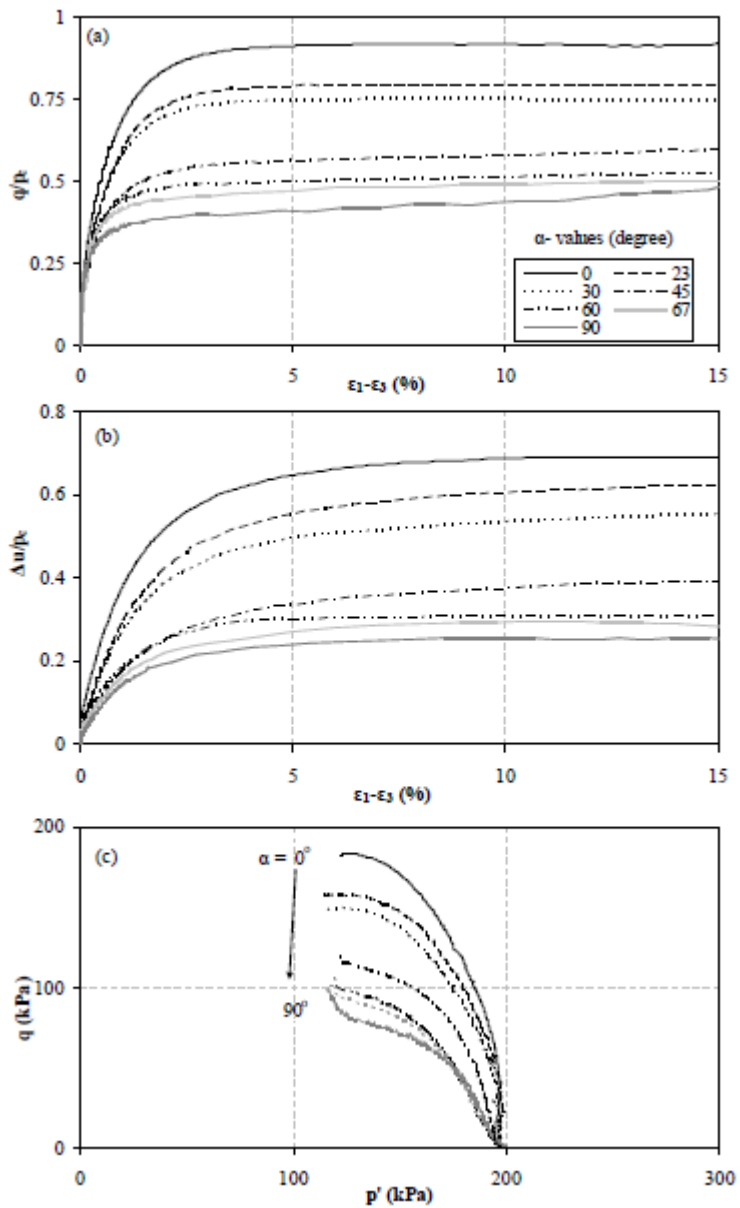


Figure 9: Measured curves of (a) normalized deviator stress ( $q/p$ ) versus shear strain ( $\epsilon_1 - \epsilon_3$ ), (b) normalized excess pore water pressure ( $\Delta u/p$ ) versus shear strain ( $\epsilon_1 - \epsilon_3$ ), (c) shear stress ( $q$ ) versus normal stress ( $p'$ ) for consolidation pressure of 200 kPa

From Figures 8 and 9, a number of characteristics are observed and are explained as follows:

- (a) The curves of the normalized deviator stress ( $q/p_c$ ) versus shear strain ( $\varepsilon_1 - \varepsilon_3$ ) increase with the decrease of consolidation pressure. The deviator stresses show a gradual ductile behaviour with the increase in shear strain. Higher deviator stresses have been observed for  $\alpha=0$  in both two consolidation pressures. The deviator stresses gradually decrease with increasing  $\alpha$ -values from  $0^\circ$  to  $90^\circ$  and the minimum deviator stresses have been observed for  $\alpha=90^\circ$ .
- (b) The curves of normalized excess pore pressure ( $\Delta u/p_c$ ) versus shear strain ( $\varepsilon_1 - \varepsilon_3$ ) show shear compression. Development of excess pore pressure ( $\Delta u$ ) decreases with the increase of major principal stress inclinations from  $0^\circ$  to  $90^\circ$ . The normalized excess pore water pressure is little bit lower under lower consolidation pressure than that under higher consolidation pressure.
- (c) Effective stress paths clearly show the decreasing of shear stress with the increase of the principal stress inclinations. The contractions of the specimens are similar in fashion for all inclinations of major principal stresses. It is important to note that the  $p'$  values at failure for all inclinations of principal stress are more or less the same.

Decreasing of deviator stresses as well as the excess pore pressures with the increase of major principal stress directions to the vertical is reported by previous researchers, (Luan et. al, 2007; Lin and Penumadu, 2005). It should be noted that the deviator stress for  $\alpha=90^\circ$  has been observed little bit higher than that for  $\alpha=60^\circ$  in Lin and Penumadu (2005). But the pore water pressure has the gradual decreasing trend with the increase of major principal stress directions.

#### 4.2 Friction Angles, Pore pressure coefficient and the Failure surface

The Mohr-Coulomb failure criterion is expressed in terms of the major and minor principal stresses as for zero effective cohesion:

$$\phi' = \sin^{-1} \left( \frac{\sigma_1' - \sigma_3'}{\sigma_1' + \sigma_3'} \right)$$

[4]

where the frictional angle  $\phi'$  is independent of intermediate principal stress  $\sigma_2'$ . In Eqn.(4), effective cohesion is assumed zero here for easy explanation. The friction angle obtained is considered to be the secant frictional angle with zero cohesion.

The failure of specimens in this test series has been considered as the peak deviatoric stress ( $q/p_c$ ) or the point of 15% shear strain. The Mohr-Coulomb friction angles measured at failure plotted with respect to the value of  $\alpha$  are shown in Figure 10. The friction angle initially increases with increasing the value of  $\alpha$  up to  $30^\circ$ , after which the friction angle decreases for  $\alpha > 30^\circ$ . The difference of friction angle is about  $9^\circ$  in the range of  $\alpha$  from  $0^\circ$  to  $90^\circ$ . Lade et al. (1994) has been reported the similar trend friction angles for sands with a variation of about  $8^\circ$ . Towhata and Ishihara (1985) using the cyclic rotation of principal stress has also been reported the similar trend that has been observed in the present study. The Skempton's pore pressure parameter,  $A_f$  at failure is shown in Figure 11. There is a monotonic increase of the  $A_f$  value with the increase of the  $\alpha$  from  $0^\circ$  to  $90^\circ$ . The maximum and minimum values of  $A_f$  have been obtained for  $\alpha = 0^\circ$  and  $\alpha = 90^\circ$ . The maximum and minimum values of  $A_f$  are consistent to the conventional triaxial compression and extension.

Most of the failure envelopes from axial torsional loading on the sedimentary soils have been shown in  $(\sigma_z - \sigma_\theta)/2$  and  $\tau_{z\theta}$  space. The failure envelope presented in  $(\sigma_z - \sigma_\theta)/2$  and  $\tau_{z\theta}$  space is simple and clear to describe the stress state of a specimen (Nishimura et al. 2007). Figure 12 shows the failure surface obtained in this test series in  $(\sigma_z - \sigma_\theta)/(2p_c)$  and  $\tau_{z\theta}/p_c$  space. The shape of the failure envelopes is similar for both the two different consolidation stresses, but has some effects of the consolidation stresses. Stress paths for higher consolidation stress are also plotted in this figure. The stress paths accurately follow the inclinations of principal stress values.

### 4.3 Comparison of Friction angles

The strength behavior of the CDG specimens in torsional shear is compared to that obtained from true triaxial compression as well as the strength from well known 3D failure criterion for soils. In torsional shear tests where inside and outside pressures are maintained at the same value, the inclination angle  $\alpha$  of the major principal stress relative to the vertical, direction is related to the parameter  $b$  as  $b = \sin^2 \alpha$ . The parameter  $b$  represents the relative magnitudes of the intermediate principal stress and expressed as  $b = (\sigma_2 - \sigma_3)/(\sigma_1 - \sigma_3)$ .

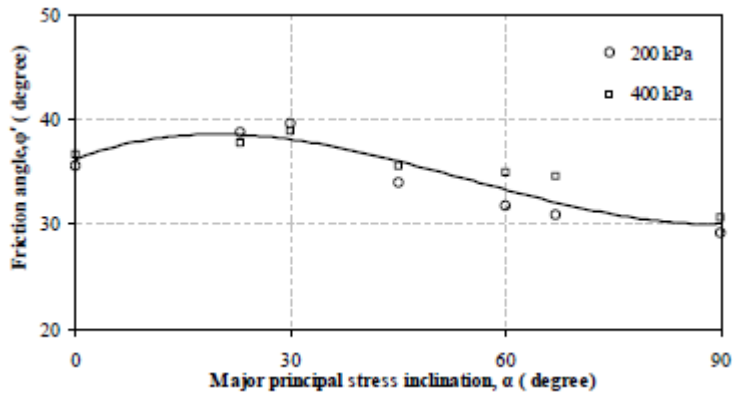


Figure 10: Secant friction angles versus major principle stress directions

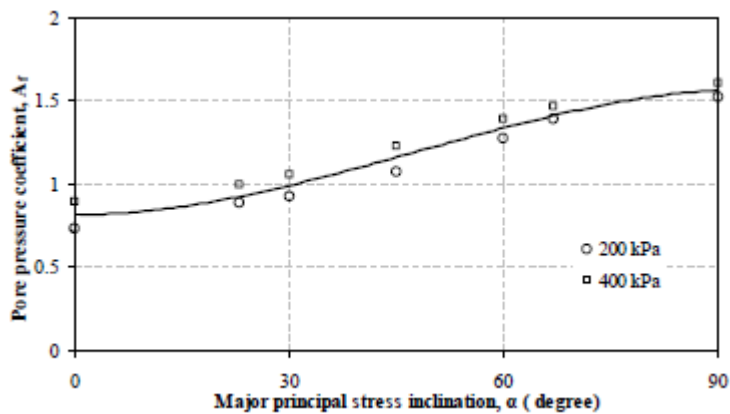


Figure 11: Pore pressure coefficient versus major principle stress directions

It should mention here that no direct comparison between these two test conditions is possible. The author wanted to find out the cause of the lowering of strength parameters in torsional shear tests at the higher angle of principal stress rotation that has been addressed in Lade et al. (2008). Figure 13 shows the friction angles measured from torsional shear tests together with the friction angles from true triaxial tests, all plotted with respect to the  $b$ -value. The true triaxial compression test results in Fig.12 represent the results in the first sector of  $\pi$  plane, that is,  $0 < \theta < 60^\circ$ , here  $\theta$  is Lode's angle Lade et al. (2008) pointed out that the effect of cross-anisotropy in true triaxial results may not be

pronounced in the first sector. The curves are also plotted using the three dimensional failure criteria for frictional materials developed by Lade and Duncan (1975). The parameter of the failure criteria was calculated using the friction angles from the same triaxial compression tests ( $\alpha=0$ ) performed on specimens consolidated at two different consolidation pressures.

The failure criterion matches the true triaxial test results better than the torsion shear tests, although the friction angles in true triaxial experiments are lower than the predicted one. The friction angles from torsional shear tests follow the predicted friction angles from triaxial compression ( $b=0.0$ ) to  $b=0.25$ . The average of friction angles in plane strain compression tests of CDG was 42.1 and the corresponding  $b$  value is 0.21, which is very close to the  $b$  value of 0.25 (shown in Figure 13). Therefore, the study confirms the findings of Lade et al.

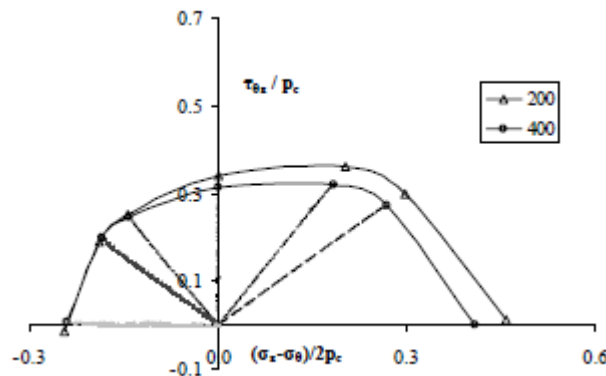


Figure 12: Failure envelope and stress paths

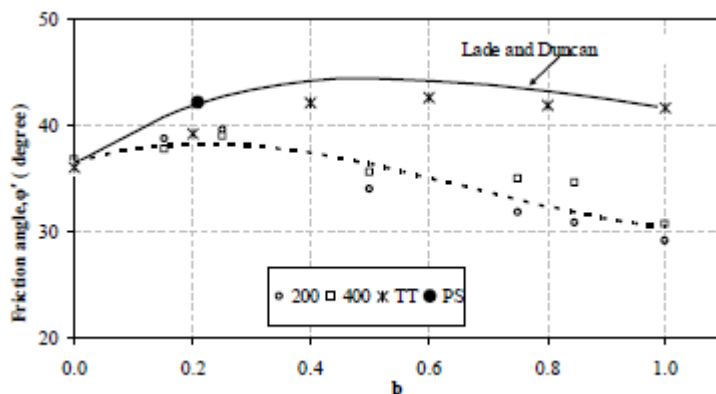


Figure 13: Comparison of friction angles of CDG in TT and HC specimens

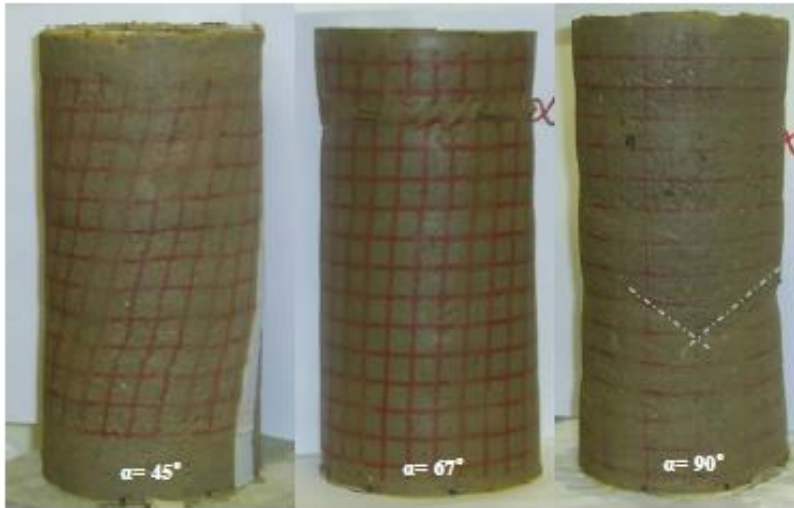


Figure 14: The tested specimens for  $\alpha = 45^\circ$ ,  $67^\circ$  and  $90^\circ$

(2008) that the strength parameters in three dimensional cases increase from triaxial compression to the plane strain condition. The dotted line in Figure 13 shows the trend line of the friction angles in torsional shear tests. The trend line is much lower than the predicted friction angles after  $b=0.25$ . This is probably due to the cross-anisotropic behaviour of completely decomposed granite or the strain localization at failure. Lade et al. (2008) pointed out this type of differences in friction angles obtained from similar tests on Santa Monica beach sand and described that the occurrence of shear banding or the cross-anisotropy may cause this lowering of friction angles for  $b$  after the condition of plane strain or  $b>0.3$ . Figure 14 shows that no visible shear band has been observed in torsional shear testing on CDG for  $b \leq 0.5$ . Strain localization occurred in the form of the necking of the specimens for  $b > 0.5$ . Therefore, the cross-anisotropy may have considerable effect to cause these strength parameters much lower in high range of  $b$  up to 0.5. The experimental results observed for higher ranges of  $b$  ( $b > 0.5$ ), cross-anisotropy together with the formation of necking may also have significant effect on the lowering of friction angles of CDG specimens. It needs more in-depth investigation of shear bands or necking rather than the visual inspection.

## 5.0 Conclusions

A laboratory study has been carried out to investigate the stress-strain-strength behaviour of completely decomposed granite (CDG) for different principal stress directions from hollow cylinder tests on specimens under consolidated undrained conditions. The influence of the principal stress direction on the strength behaviour of CDG was compared with the result obtained from the same CDG soil in true triaxial condition. It is observed that the deviator stresses as well as excess pore pressures decrease with the increase of principal stress directions. Shear strength parameters and the coefficient of pore pressures are also affected by the inclinations of the principal stress. Significant influence of consolidation pressures have been observed on the failure of the soil. Friction angle initially increases with the increase of the principal stress inclination up to  $30^\circ$ . After that, a gradual decrease of the friction angle has been obtained for higher range of inclinations from  $30^\circ$  to  $90^\circ$ . Comparison of strength parameters in principal stress rotation with that of true triaxial testing shows pronounced effects of cross-anisotropy for inclinations higher than  $30^\circ$ . Strain localizations may also have contributed to lower strength parameters of the soil in the higher range of inclinations.

## Acknowledgements

Financial supports from The Hong Kong Polytechnic University and a grant from Research Grants Committee (RGC: PolyU 5174/04E) of the Hong Kong Special Administrative Region Government of China are gratefully acknowledged.

## References

- Albert, C., Zdravkovic, and Jardine, R.J. (2003). Behaviour of Bothkennar clay under rotation of principal stresses. Int. Workshop on Geotechnics of Soft Soils-Theory and Practice. Vermeer, Schweiger, Karstunen and Cundny, eds. VGE, pp.1-6.
- Broms, B.B. and Casbarian, A.O. (1965). Effects of rotation of the principal stress axes and of the intermediate principal stress on the shear strength. In: Proceedings of the 6th ICSMFE, Montreal, Vol.1, pp. 179–183.
- GCTS (2007). See website [www.gcts.com](http://www.gcts.com).
- Hong, W.P. and Lade, P.V. (1989). Elasto-plastic behaviour of  $K_0$  consolidated clay in torsional shear tests. *Soils and Foundations*, Vol. 29, No.2, pp.127-140

- Lade P.V., Ghaboussi, J., Inel, S., and Yamamuro, J.A. (1994). Experimental determination of constitutive behaviour of soils. Proceedings of the 8th International Conference on Association of Computer Methods for Advances in Geomechanics. pp.215-222.
- Lade, P.V. and Duncan, J.M. (1975). Elastoplastic stress-strain theory for cohesionless soil. *Journal of the Geotechnical Engineering Division, ASCE*, 101(GT10): 1037-1053.
- Lade, P.V., Nam, J., and Hong, W.P. (2008). Shear banding and cross-anisotropic behaviour observed in laboratory sand tests with stress rotation. *Canadian Geotechnical Journal*, Vol.45 pp.74-84.
- Lin, H. and Penumadu, D. (2002). Interpretation of combined axial-torsional test for 3D constitutive behaviour of geo-materials. 15th ASCE Engineering Mechanics Conference, June 2-5, Columbia University, NY, pp.1-8.
- Lin, H. and Penumadu, D. (2005). Experimental investigation of principal stress rotation in kaolin clay. *Journal of Geotechnical and Geoenvironmental Engineering*, Vol.131, No.5, pp.633-642.
- Luan, M., Xu, C., He, Y., Guo, Y., Zhang, Z., Jin, D., and Fan, Q. (2007). Experimental study on shear behaviour and an improved constitutive model of saturated sand under complex stress condition. *Soft Soil Engineering*, Chan and Law, eds. pp.73-92.
- Mandeville, D. and Penumadu, D. (2004). True triaxial testing system for clay with proportional-integral-differential (PID) control. *Geotechnical Testing Journal*, ASTM Vol.27, No.2, pp.1-11.
- Miura, K., Miura, S., and Toki, S. (1986). Deformation behaviour of anisotropic dense sand under principal stress axes rotation. *Soils and Foundations*, Vol.26, No.1, pp.36-52.
- Nishimura, S., Minh, N.A., and Jardine, R.J. (2007). Strength anisotropy of natural London clay. *Geotechnique*, Vol.57, No.1, pp.49-62.
- Saada, A.S. and Zamani, K.K. (1969). The mechanical behavior of cross anisotropic clays. In: Proceedings of the 7th *ICSMFE*, Mexico, Vol.1, pp.351-359.
- Saada, A.S. (1988). State of the art: Hollow cylinder torsional devices: their advantages and limitations. *Advance triaxial testing of soil and rock*. ASTM STP 977, R.T. Donaghe, R.C. Chaney, and M.L. Silver, eds., *American Society for Testing and Materials*, Philadelphia, pa., pp.766-795.
- Saada, A.S. and Townsend, F.C. (1980). State of the art: Laboratory strength testing of soils, *Laboratory Shear Strength of Soil*, ASTM STP 740, R.N. Yong and F.C. Townsend, eds., *American Society for Testing and Materials*, Philadelphia, pa., pp.7-77.
- Towhata, I. and Ishihara, K. (1985). Undrained strength of sand undergoing cyclic rotation of principal stress axes. *Soils and Foundations*, Vol. 25, No.2, pp.135-147.